Article

Suppressed phase segregation for triple-junction perovskite solar cells

https://doi.org/10.1038/s41586-023-06006-7

Received: 30 October 2022

Accepted: 23 March 2023

Published online: 28 March 2023

Check for updates

Zaiwei Wang[1,12], Lewei Zeng[1,12], Tong Zhu[1,12], Hao Chen[1,12], Bin Chen[1,2], Dominik J. Kubicki[3], Adam Balvanz[2], Chongwen Li[1,4], Aidan Maxwell[1], Esma Ugur[5], Roberto dos Reis[6], Matthew Cheng[6], Guang Yang[7], Biwas Subedi[4], Deying Luo[8], Juntao Hu[9], Junke Wang[1], Sam Teale[1], Suhas Mahesh[1], Sasa Wang[1], Shuangyan Hu[1], Eui Dae Jung[1], Mingyang Wei[1,10], So Min Park[1], Luke Grater[1], Erkan Aydin[5], Zhaoning Song[4], Nikolas J. Podraza[4], Zheng-Hong Lu[8,9], Jinsong Huang[7], Vinayak P. Dravid[6], Stefaan De Wolf[5], Yanfa Yan[4], Michael Grätzel[10], Merx G. Kanatzidis[2] & Edward H. Sargent[1,2,11] ✉

The tunable bandgaps and facile fabrication of perovskites make them attractive for multi-junction photovoltaics[1,2]. However, light-induced phase segregation limits their efficiency and stability[3–5]: this occurs in wide-bandgap (>1.65 electron volts) iodide/bromide mixed perovskite absorbers, and becomes even more acute in the top cells of triple-junction solar photovoltaics that require a fully 2.0-electron-volt bandgap absorber[2,6]. Here we report that lattice distortion in iodide/bromide mixed perovskites is correlated with the suppression of phase segregation, generating an increased ion-migration energy barrier arising from the decreased average interatomic distance between the A-site cation and iodide. Using an approximately 2.0-electron-volt rubidium/caesium mixed-cation inorganic perovskite with large lattice distortion in the top subcell, we fabricated all-perovskite triple-junction solar cells and achieved an efficiency of 24.3 per cent (23.3 per cent certified quasi-steady-state efficiency) with an open-circuit voltage of 3.21 volts. This is, to our knowledge, the first reported certified efficiency for perovskite-based triple-junction solar cells. The triple-junction devices retain 80 per cent of their initial efficiency following 420 hours of operation at the maximum power point.

Multi-junction solar cells offer routes to increase power conversion efficiency (PCE) by stacking multiple light-absorbing layers with complementary bandgaps and minimizing charge-carrier thermalization losses[7,8]. Halide perovskites with tunable bandgaps, long charge-carrier diffusion lengths, high light-harvesting efficiency and facile fabrication are compelling materials for multi-junction photovoltaics[1,2,9–14]. However, the challenge of light-induced phase segregation (LIPS) for wide-bandgap (>1.65 electron volts (eV)) iodide/bromide (I/Br) mixed perovskite absorbers in the top subcells limits the PCE and stability of perovskite-based multi-junction photovoltaics, especially triple-junction solar cells (TJSCs)[2–4,6,15]. Perovskite-based TJSCs, such as all-perovskite, perovskite/perovskite/silicon and perovskite/perovskite/CuInGa(Se,S), have a higher theoretical PCE than their double- and single-junction counterparts[2,16]. Nevertheless, so far, perovskite-based TJSCs have achieved an efficiency of only 20.1%, a PCE that decreases to about 5% after 1 h of continuous operation[6,17–19] (Supplementary Table 1).

We noted that most previously reported I/Br mixed perovskite compositions exhibiting suppressed LIPS have enlarged lattice distortions: these have been achieved through doping with smaller A-site cations, and also by increasing the larger X-site iodide anion content[3,4,20–26]. On the basis of this observation, we hypothesized that increasing lattice distortion raises the ion-migration energy barrier, thereby suppressing LIPS (Fig. 1a). For a similar range of bandgaps, caesium (Cs)-based inorganic perovskites, with a smaller A-site cation and a higher iodide anion content, have a higher degree of lattice distortion and better stability under illumination than organic–inorganic hybrid perovskites[1,27,28]. However, 2.0-eV-bandgap Cs-based inorganic perovskites, such as $CsPbI_{1.4}Br_{1.6}$ (Supplementary Fig. 1), as the absorber in the top subcell for perovskite-based TJSCs still face the challenge of LIPS under illumination[22].

We find that rubidium (Rb), which has a smaller cation radius than Cs, can be doped into the inorganic perovskite lattice and that the upper limit of Rb doping content is positively correlated with the Br

[1]Department of Electrical and Computer Engineering, University of Toronto, Toronto, Ontario, Canada. [2]Department of Chemistry, Northwestern University, Evanston, IL, USA. [3]Department of Physics, University of Warwick, Coventry, UK. [4]Department of Physics and Astronomy and Wright Center for Photovoltaics Innovation and Commercialization, The University of Toledo, Toledo, OH, USA. [5]KAUST Solar Center (KSC), Physical Sciences and Engineering Division (PSE), King Abdullah University of Science and Technology (KAUST), Thuwal, Kingdom of Saudi Arabia. [6]Department of Materials Science and Engineering, Northwestern University, Evanston, IL, USA. [7]Department of Applied Physical Sciences, University of North Carolina at Chapel Hill, Chapel Hill, NC, USA. [8]Department of Materials Science and Engineering, University of Toronto, Toronto, Ontario, Canada. [9]Department of Physics, Center for Optoelectronics Engineering Research, Yunnan University, Kunming, China. [10]Laboratory of Photonics and Interfaces, Institute of Chemical Sciences and Engineering, Ecole Polytechnique Fedérale de Lausanne (EPFL), Lausanne, Switzerland. [11]Department of Electrical and Computer Engineering, Northwestern University, Evanston, IL, USA. [12]These authors contributed equally: Zaiwei Wang, Lewei Zeng, Tong Zhu, Hao Chen. ✉e-mail: ted.sargent@utoronto.ca

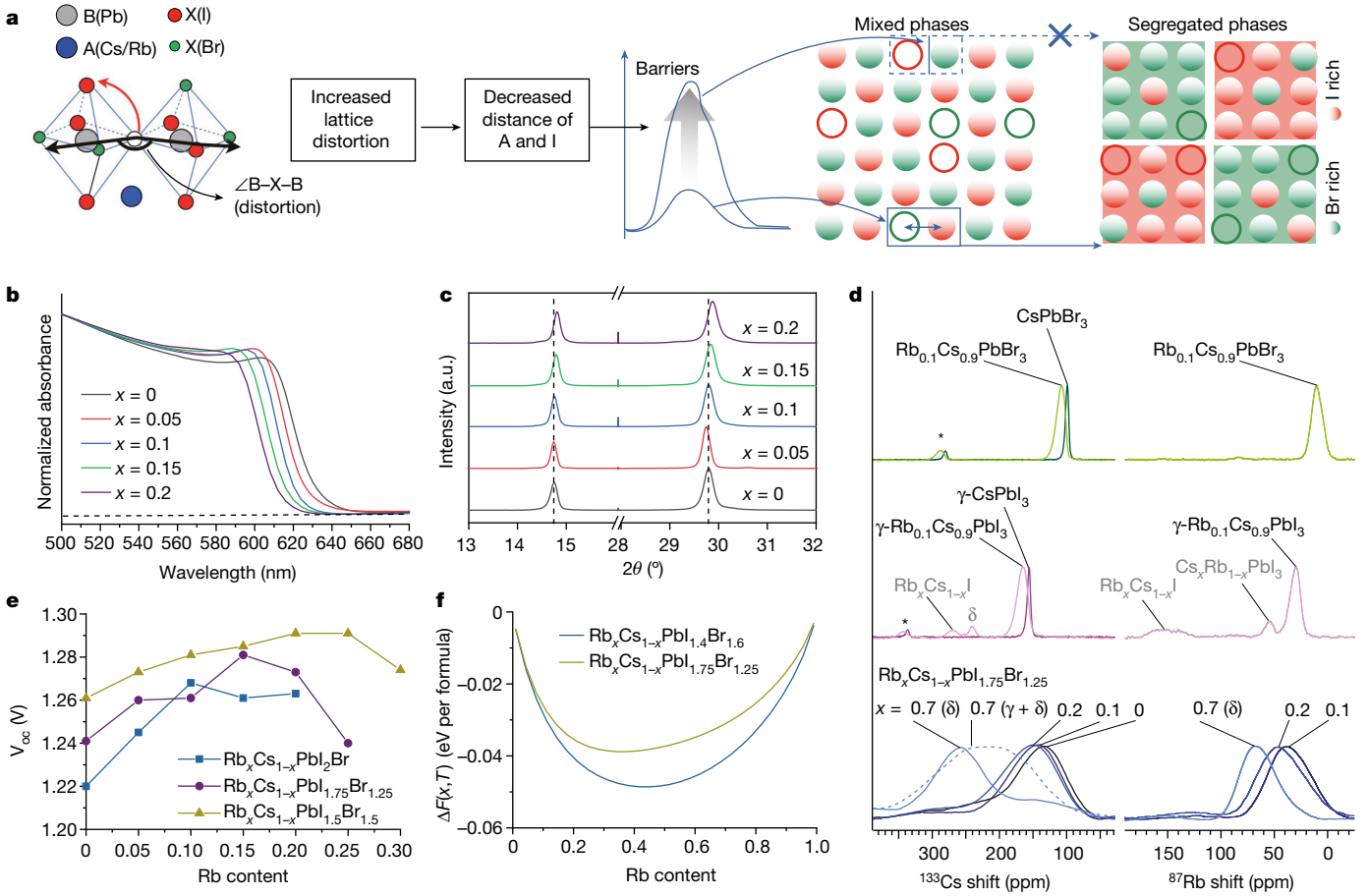

Fig. 1 | Properties of Rb/Cs mixed-cation inorganic perovskites. **a**, Schematic illustration of the suppression mechanism of LIPS. The hollow circles denote vacancies. **b**,**c**, UV–vis absorption spectra (**b**) and XRD patterns (**c**) of $Rb_xCs_{1-x}PbI_{1.75}Br_{1.25}$ ($x = 0$, 0.05, 0.1, 0.15, 0.2). θ is the angle of diffraction. **d**, ^{133}Cs and ^{87}Rb solid-state MAS NMR spectra of Rb-doped caesium lead halides recorded at 20 T, 20 kHz MAS and room temperature. The green, purple and blue lines represent pure-I, pure-Br and mixed-I/Br phases. The δ and γ symbols indicate the hexagonal non-perovskite and 3 three-dimensional perovskite polymorphs, respectively. The light grey labels indicate secondary phases coexisting in small quantities with the main phase. The asterisks indicate spinning sidebands. **e**, The V_{OC} as a function of Rb doping content for the single-junction solar cells of $Rb_xCs_{1-x}PbI_2Br$, $Rb_xCs_{1-x}PbI_{1.75}Br_{1.25}$ and $Rb_xCs_{1-x}PbI_{1.5}Br_{1.5}$. **f**, The DFT-calculated Helmholtz free energy ΔF (can be treated as a thermodynamic driving force) with different Rb doping content in $Rb_xCs_{1-x}PbI_{1.4}Br_{1.6}$ and $Rb_xCs_{1-x}PbI_{1.75}Br_{1.25}$ (see Methods for details). x, Rb content; T, temperature. T = 300 K.

content. Rb^+ lattice doping widens the bandgap of inorganic perovskites, meaning that Rb/Cs solid solutions require a higher I content to achieve a bandgap of about 2.0 eV (such as $Rb_{0.15}Cs_{0.85}PbI_{1.75}Br_{1.25}$, compared with about 2.0 eV $CsPbI_{1.4}Br_{1.6}$). The approximately 2.0-eV Rb/Cs mixed-cation inorganic perovskites with a larger degree of lattice distortion than their Cs-based counterparts show suppressed LIPS because of the decreased average interatomic distance between the A-site cation (where A is Cs or Rb) and I, and the increased energy barrier of halide ion migration. Finally, we applied the approximately 2.0-eV Rb/Cs perovskites in all-perovskite TJSCs and achieved an efficiency of 24.3% (23.29% certified quasi-steady-state efficiency). Our all-perovskite TJSC retains 80% of its initial efficiency after 420 h of operation at maximum power point under room temperature and air mass 1.5 global (AM 1.5G) 1-sun illumination.

Rb/Cs mixed-cation inorganic perovskites

We partially replaced Cs^+ with Rb^+ in a Cs-based I/Br mixed inorganic perovskite $CsPbI_{1.75}Br_{1.25}$. Ultraviolet–visible (UV–Vis) absorption spectra (Fig. 1b and Supplementary Fig. 2) show a gradual blueshift of the absorption edge from 631 nm for the pure Cs-based perovskite $CsPbI_{1.75}Br_{1.25}$ to 614 nm for the Rb/Cs mixed-cation perovskite $Rb_{0.2}Cs_{0.8}PbI_{1.75}Br_{1.25}$. From X-ray diffraction (XRD), we find that Rb can be doped into the $CsPbI_{1.75}Br_{1.25}$ lattice to form a pure perovskite phase in $Rb_xCs_{1-x}PbI_{1.75}Br_{1.25}$ ($x \leq 0.2$) films (Fig. 1c and Supplementary Fig. 2). For pure-halide Rb/Cs mixed-cation films, $Rb_xCs_{1-x}PbBr_3$ ($x \leq 0.7$) and $Rb_xCs_{1-x}PbI_3$ ($x \leq 0.1$) are pure perovskite phases (see Supplementary Note 1 for a detailed discussion). Thus, the upper limit of Rb lattice-doping content for retaining a pure perovskite phase is positively correlated with the Br content in these Rb/Cs mixed-cation materials.

Solid-state nuclear magnetic resonance (NMR) spectroscopy is used to study dopants in halide perovskites[29,30]. We carried out solid-state magic-angle spinning (MAS) NMR measurements on materials prepared by mechanosynthesis to study the local structure of ^{133}Cs and ^{87}Rb. Upon Rb^+ doping of single-halide and mixed-halide inorganic perovskites, the ^{133}Cs perovskite peaks broaden and shift to higher frequencies. The ^{87}Rb spectra show peaks corresponding to Rb^+ inside the perovskite phase. These observations corroborate that Rb^+ can be incorporated into Cs-based inorganic perovskites (Fig. 1d, Supplementary Figs. 3–5 and Supplementary Notes 2 and 3 for a detailed discussion)[29].

Rb/Cs mixed-cation perovskites with a bandgap near 2.0 eV (Supplementary Fig. 6 and Supplementary Tables 2–4) including $Rb_xCs_{1-x}PbI_2Br$ ($x = 0$, 0.05, 0.1, 0.15, 0.2), $Rb_xCs_{1-x}PbI_{1.75}Br_{1.25}$ ($x = 0$, 0.05, 0.1, 0.15, 0.2, 0.25) and $Rb_xCs_{1-x}PbI_{1.5}Br_{1.5}$ ($x = 0$, 0.1, 0.15, 0.2, 0.25, 0.3) were employed as the absorbers in perovskite solar cells (PSCs). Devices with perovskite

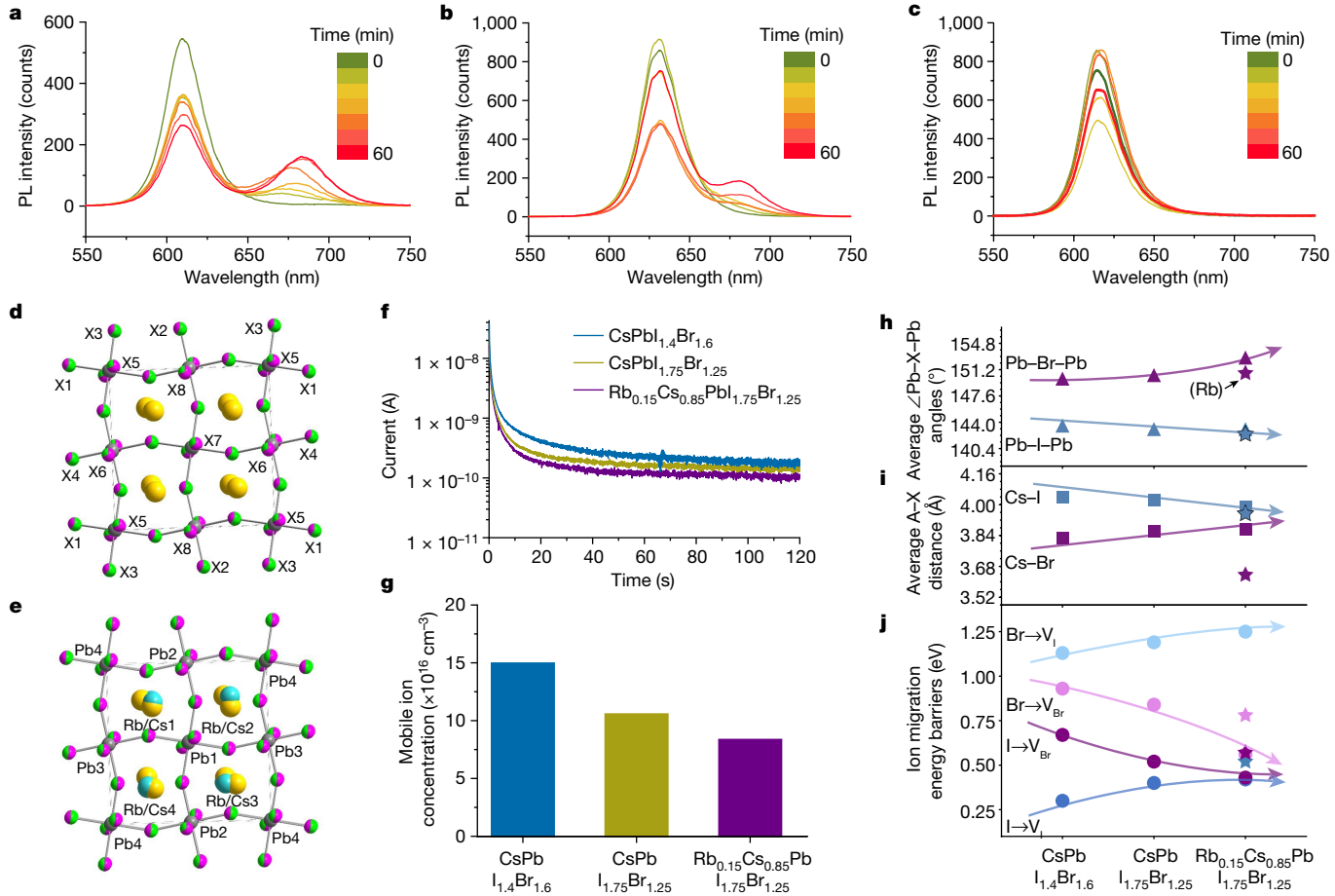

Fig. 2 | The phenomena and mechanism of suppressed LIPS. a–**c**, PL spectra of $CsPbI_{1.4}Br_{1.6}$ (**a**), $CsPbI_{1.75}Br_{1.25}$ (**b**) and $Rb_{0.15}Cs_{0.85}PbI_{1.75}Br_{1.25}$ (**c**) perovskite films under 1-sun AM 1.5G illumination for 60 min. **d**,**e**, The structures of the crystals from the loading compositions $CsPbI_{1.4}Br_{1.6}$ and $CsPbI_{1.75}Br_{1.25}$ (**d**) and $Rb_{0.15}Cs_{0.85}PbI_{1.75}Br_{1.25}$ (**e**) as viewed down the crystallographic *b* axis. The halide positions are labelled by X (where X is I or Br), and the labelling scheme for the atoms is consistent between the two structures. The Rb, Cs, Pb, I and Br atoms are labelled in blue, yellow, grey, pink and green, respectively. The fractional occupancy of the halide sites is shown as partially filled sectors. Halide sites X1–X4 propagate in the *a*–*c* plane, and halide sites X5–X8 propagate down the *b* axis. **f**,**g**, Transient ion-migration currents (**f**) and calculated mobile ion concentrations (**g**) of $CsPbI_{1.4}Br_{1.6}$, $CsPbI_{1.75}Br_{1.25}$ and $Rb_{0.15}Cs_{0.85}PbI_{1.75}Br_{1.25}$ PSCs. **h**–**j**, DFT-calculated average ∠Pb–X–Pb (where X is I or Br) (**h**), average A···X interatomic distance (**i**) and ion-migration energy barrier of I (or Br) to V_I (or V_{Br}) (**j**) for $CsPbI_{1.4}Br_{1.6}$, $CsPbI_{1.75}Br_{1.25}$ and $Rb_{0.15}Cs_{0.85}PbI_{1.75}Br_{1.25}$. The arrows represent their trends. For $Rb_{0.15}Cs_{0.85}PbI_{1.75}Br_{1.25}$, the information around the Rb atoms is labelled with stars. Owing to the supercell limitations, the real compositions used in calculations are $CsPbI_{1.375}Br_{1.625}$ (for $CsPbI_{1.4}Br_{1.6}$), $CsPbI_{1.75}Br_{1.25}$ (for $CsPbI_{1.75}Br_{1.25}$) and $Rb_{0.125}Cs_{0.875}PbI_{1.75}Br_{1.25}$ (for $Rb_{0.15}Cs_{0.85}PbI_{1.75}Br_{1.25}$).

absorbers of $x = 0.1$ in $Rb_xCs_{1-x}PbI_2Br$, $x = 0.15$ in $Rb_xCs_{1-x}PbI_{1.75}Br_{1.25}$ and $x = 0.2$ in $Rb_xCs_{1-x}PbI_{1.5}Br_{1.5}$ show the highest open-current voltage (V_{OC}) (Fig. 1e and Supplementary Tables 2–4). Among the various absorber compositions, $Rb_{0.15}Cs_{0.85}PbI_{1.75}Br_{1.25}$ has a bandgap of about 2.0 eV (Supplementary Table 3) and delivers the highest V_{OC} in PSCs compared with other Rb-doped inorganic perovskites with a bandgap of ≤2.0 eV (Supplementary Tables 2–4). We therefore used $Rb_{0.15}Cs_{0.85}PbI_{1.75}Br_{1.25}$ as our target approximately 2.0-eV Rb/Cs mixed-cation perovskite sample in the following context. We also chose a Cs-based perovskite $CsPbI_{1.4}Br_{1.6}$ with the same approximately 2.0-eV bandgap and a Cs-based perovskite $CsPbI_{1.75}Br_{1.25}$ with the same I/Br ratio as control samples compared with the target sample.

The top-view scanning electron microscopy images in Supplementary Fig. 7 show that the $CsPbI_{1.4}Br_{1.6}$, $CsPbI_{1.75}Br_{1.25}$ and $Rb_{0.15}Cs_{0.85}PbI_{1.75}Br_{1.25}$ perovskite films are uniform and pinhole-free. These films also have a low root-mean-square roughness (<26 nm), as shown in atomic force microscopy images (Supplementary Fig. 7). The energy-dispersive X-ray spectroscopy mapping and depth-profile X-ray photoelectron spectroscopy of $Rb_{0.15}Cs_{0.85}PbI_{1.75}Br_{1.25}$ films (Supplementary Figs. 8–10) show a uniform distribution of Rb at the surface and throughout the depth of the perovskite films.

Density functional theory (DFT) calculations reveal a deeper Helmholtz free energy (larger thermodynamic driving force) for Rb/Cs mixed-cation perovskites with an increase in Br content (Fig. 1f). In addition, the Rb content is also correlated with the phase stability (Supplementary Figs. 4 and 5 and Supplementary Note 2 for a detailed discussion)[31]. Thus, we attribute the positive correlation between the upper limit of Rb doping content and the Br content in inorganic perovskites to the increase in thermodynamic driving force and the relatively stable perovskite phase in Br-rich perovskites.

Suppressed LIPS

We carried out time-dependent photoluminescence (PL) measurements of encapsulated $CsPbI_{1.4}Br_{1.6}$, $CsPbI_{1.75}Br_{1.25}$ and $Rb_{0.15}Cs_{0.85}PbI_{1.75}Br_{1.25}$ perovskite films under 1-sun illumination (AM 1.5G). The initial PL spectrum of $CsPbI_{1.4}Br_{1.6}$ shows a PL peak at 610 nm (Fig. 2a). A new lower-energy PL peak at about 680 nm appears after 10 min owing to LIPS. With the extension of illumination time, the intensity of the peak at about 680 nm increases, and simultaneously the initial peak at about 610 nm decreases in intensity. The initial PL peak of the $CsPbI_{1.75}Br_{1.25}$ film is at 630 nm, and a lower-energy PL peak at about 680 nm appears

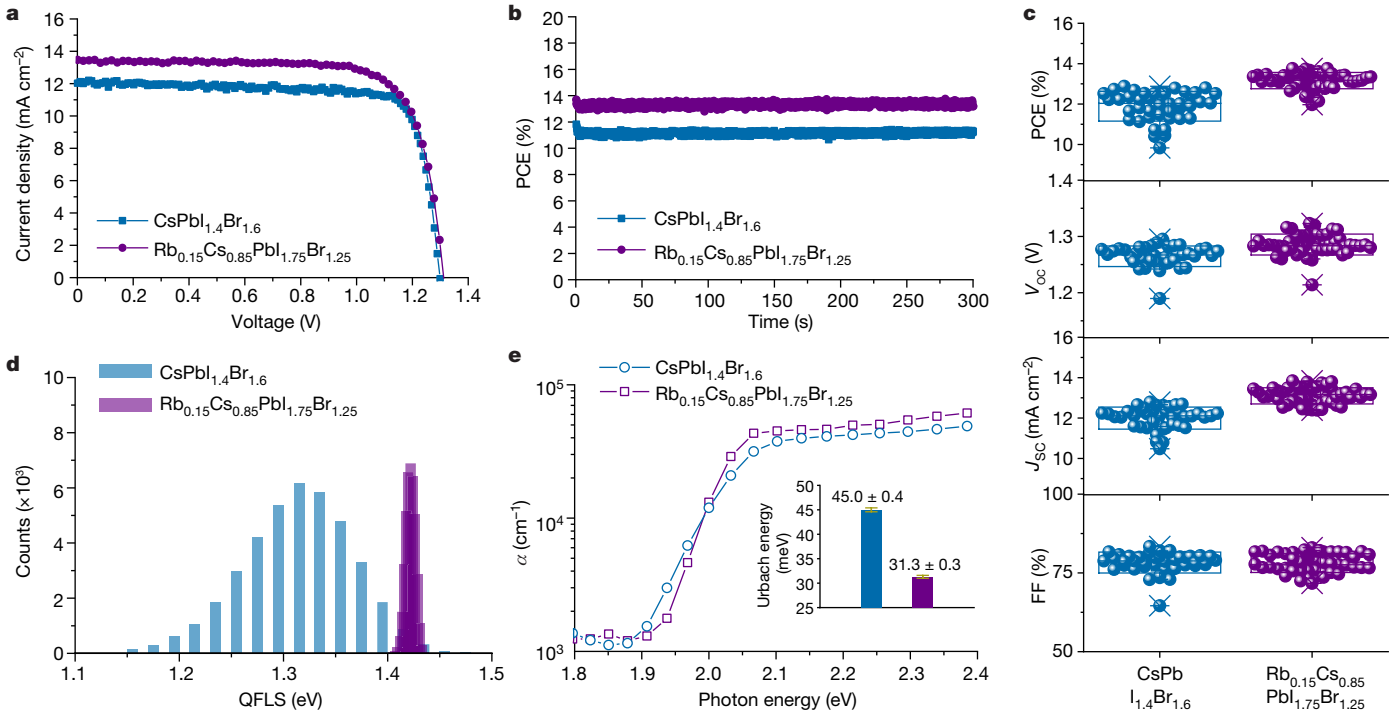

Fig. 3 | PV performance of 2.0-eV single-junction PSCs. a,**b**, *J*–*V* curves (**a**) and SPO (**b**) of approximately 2.0-eV $CsPbI_{1.4}Br_{1.6}$ and $Rb_{0.15}Cs_{0.85}PbI_{1.75}Br_{1.25}$ PSCs. **c**, Statistics of PCE, V_{OC}, J_{SC} and FF of the $CsPbI_{1.4}Br_{1.6}$ devices (41 samples) and the $Rb_{0.15}Cs_{0.85}PbI_{1.75}Br_{1.25}$ devices (54 samples). **d**, Histogram of QFLS pixel values of $CsPbI_{1.4}Br_{1.6}$ and $Rb_{0.15}Cs_{0.85}PbI_{1.75}Br_{1.25}$ perovskites taken from larger 100 μm × 100 μm images. **e**, Near-bandgap absorption coefficient (α) spectra from PDS for $CsPbI_{1.4}Br_{1.6}$ and $Rb_{0.15}Cs_{0.85}PbI_{1.75}Br_{1.25}$ thin films. Inset: Urbach energy extracted from the PDS measurements.

after 30 min of illumination (Fig. 2b). After 60 min of illumination, the $CsPbI_{1.75}Br_{1.25}$ film shows a lower PL intensity of the peak at about 680 nm than the $CsPbI_{1.4}Br_{1.6}$ film. Our target sample, $Rb_{0.15}Cs_{0.85}PbI_{1.75}Br_{1.25}$, which exhibits an initial PL peak at about 616 nm, shows a negligible peak shift (less than 2 nm) and an absence of a lower-energy peak after 60 min of illumination (Fig. 2c). These results indicate that the $CsPbI_{1.75}Br_{1.25}$ films with a higher iodide content undergo weaker LIPS than do $CsPbI_{1.4}Br_{1.6}$ films, and that approximately 2.0-eV Rb/Cs mixed-cation perovskites show the best light stability among these. The spatial homogeneity of the PL peak position agrees with this finding (Supplementary Fig. 11).

To study the mechanism of LIPS suppression in Rb/Cs mixed-cation perovskites, we grew single crystals in solid-state reactions with the loading compositions $CsPbI_{1.4}Br_{1.6}$, $CsPbI_{1.75}Br_{1.25}$ and $Rb_{0.15}Cs_{0.85}PbI_{1.75}Br_{1.25}$, and analysed their single-crystal diffraction data. All compounds crystallize in a monoclinic crystal system best described by the $P2_1/m$ space group (Fig. 2d,e, Supplementary Figs. 12–14, Supplementary Table 5 and Supplementary Notes 4 and 5 for a detailed discussion). These structures exist as a supercell (Supplementary Fig. 12 and Supplementary Note 4 for a detailed discussion), presumably because of the partial ordering of the halides. To our knowledge, this has not yet been reported in the literature. The single-crystal XRD data unambiguously show that Rb substitutes Cs on the A site.

Substituting Rb at the Cs site leads to increased lattice distortions as evidenced by the decrease in the Pb–X–Pb (where X is I/Br mixed sites) bond angles (∠Pb–X–Pb) and the widening of the bandgap when comparing $Rb_{0.15}Cs_{0.85}PbI_{1.75}Br_{1.25}$ versus $CsPbI_{1.75}Br_{1.25}$ (Supplementary Fig. 15 and Supplementary Tables 6 and 7)[32,33]. The Pb–X–Pb angles in $CsPbI_{1.75}Br_{1.25}$ show a slight increasing distortion compared with those of $CsPbI_{1.4}Br_{1.6}$ (Supplementary Table 7 and Supplementary Notes 6 and 7 for a detailed discussion).

We further estimated the concentration of mobile ions using a mobile ion charging–discharging method that has demonstrated consistency with ion-migration energy barriers[34,35]. The typical transient currents in devices are shown in Fig. 2f and the calculated average mobile ion concentrations are summarized in Fig. 2g. The mobile ion concentrations decrease from 1.45×10^{17} cm^{-3} for the $CsPbI_{1.4}Br_{1.6}$ device to 1.01×10^{17} cm^{-3} for the $CsPbI_{1.75}Br_{1.25}$ device and 7.89×10^{16} cm^{-3} for the $Rb_{0.15}Cs_{0.85}PbI_{1.75}Br_{1.25}$ device.

To explore further the distortion of the I or Br sites, we analysed the DFT-relaxed structures of $CsPbI_{1.4}Br_{1.6}$, $CsPbI_{1.75}Br_{1.25}$ and $Rb_{0.15}Cs_{0.85}PbI_{1.75}Br_{1.25}$. The average ∠Pb–I–Pb decreases from 143.54° for $CsPbI_{1.4}Br_{1.6}$ to 143.06° for $CsPbI_{1.75}Br_{1.25}$ and then decreases further to 143.05° for I far away from Rb and 142.39° for I close to Rb in $Rb_{0.15}Cs_{0.85}PbI_{1.75}Br_{1.25}$, which is indicative of increased distortion of the I site with the introduction of I or Rb (Fig. 2h and Supplementary Figs. 16 and 17). Lattice distortion results in a large variation for interatomic distances of A-site cation and X-site anion (A···X) compared with Pb···X interatomic distances (Supplementary Tables 8 and 9). Thus, we mainly focus on discussing the A···X interatomic distances in the text. The average Cs···I interatomic distance decreases from 4.04 Å for $CsPbI_{1.4}Br_{1.6}$ to 4.02 Å for $CsPbI_{1.75}Br_{1.25}$. For $Rb_{0.15}Cs_{0.85}PbI_{1.75}Br_{1.25}$, the average interatomic distance further decreases to 3.98 Å for Cs and I, and 3.95 Å for Rb and I (Fig. 2i and Supplementary Fig. 17). The energy barrier of I migrating to an I vacancy (V_I) increases from 0.33 eV for $CsPbI_{1.4}Br_{1.6}$ to 0.40 eV for $CsPbI_{1.75}Br_{1.25}$ (Fig. 2j and Supplementary Figs. 18 and 19). In addition, the migration energy barriers for $Rb_{0.15}Cs_{0.85}PbI_{1.75}Br_{1.25}$ are further increased to 0.42 eV for V_I far from Rb and 0.51 eV for V_I close to Rb.

The average A···I interatomic distance is longer than that of A···Br, and the migration energy barrier of I to V_I is the lowest among all four studied ion-migration transitions (Fig. 2i,j). In addition, the defect formation energy of V_I is lower than that of V_{Br} based on our calculations (Supplementary Fig. 20). Thus, the migration energy barriers of these materials are dominated by that of I to V_I and increase with the introduction of I and Rb. This also indicates that the most mobile ions arise from I to V_I migration, consistent with previous reports[34].

Thus, we conclude that increasing the lattice distortion in I/Br mixed inorganic perovskites increases the I-site distortion. This is associated with a decrease in the average A···I interatomic distance, which

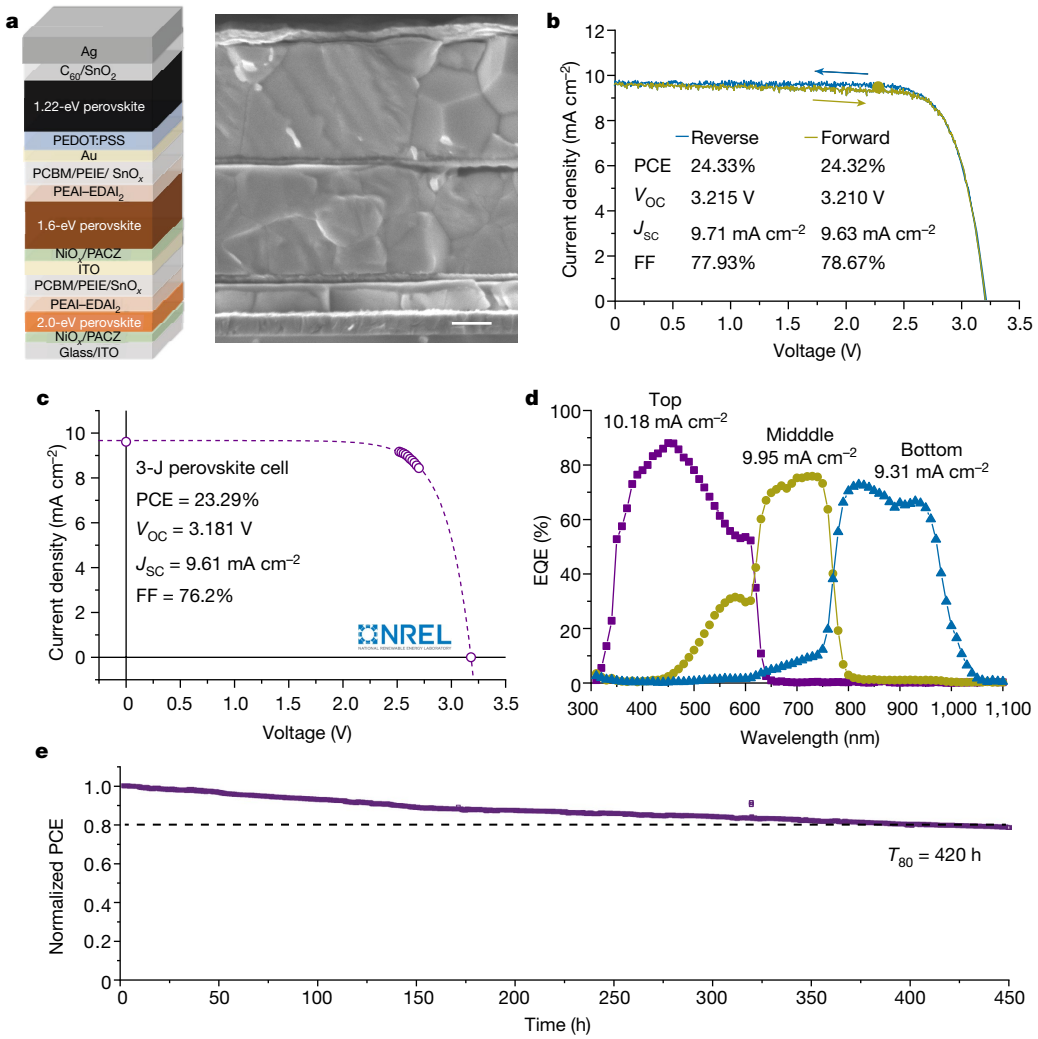

Fig. 4 | PV performance and stability of all-perovskite TJSCs. a, Schematic diagram of device structure and corresponding cross-sectional scanning electron microscopy image of the all-perovskite TJSC. Scale bar, 400 nm. **b**, *J*–*V* curves of reverse and forward scans for a champion all-perovskite TJSC. The *J*–*V* performances of the single-junction cells in all-perovskite triple-junction solar cells based on Ag electrodes are shown in Supplementary Table 10. **c**, NREL-certified quasi-steady-state *J*–*V* curve of the all-perovskite triple-junction device. **d**, EQE curves of the approximately 2.0-eV, approximately 1.6-eV and approximately 1.22-eV subcells within the TJSC. **e**, The maximum-power-point stability tracking of an encapsulated TJSC at room temperature under simulated AM 1.5G 1-sun illumination. T_{80} is the time taken for device efficiency to reduce to 80% of its initial value.

enhances the ion-migration energy barrier and suppresses ion migration and LIPS. This conclusion also offers a more comprehensive explanation for the reported phenomena of suppressed LIPS (Supplementary Note 8 for a detailed discussion).

2.0-eV single-junction PSCs

As approximately 2.0-eV perovskites are ideal absorbers as the top subcells in all-perovskites TJSCs, we compared the performance of approximately 2.0-eV $CsPbI_{1.4}Br_{1.6}$ and $Rb_{0.15}Cs_{0.85}PbI_{1.75}Br_{1.25}$ devices based on the p–i–n configuration of indium tin oxide (ITO)/nickel oxide (NiO_x)/[4-(3,6-dimethyl-9H-carbazol-9-yl)butyl]phosphonic acid (Me-4PACz)/perovskite/phenethylammonium iodide and ethane-1,2-diammonium iodide (PEAI–$EDAI_2$)/phenyl C61 butyric acid methyl ester (PCBM)/polyethyleneimine ethoxylated (PEIE)/tin oxide (SnO_x)/silver (Ag) (Supplementary Fig. 21). For the control 2.0-eV $CsPbI_{1.4}Br_{1.6}$ device, the PCE is 12.59% with a V_{OC} of 1.288 V (Fig. 3a). The PCE of the $Rb_{0.15}Cs_{0.85}PbI_{1.75}Br_{1.25}$ device increases to 13.41% with a V_{OC} of 1.312 V. Their stabilized power output (SPO) efficiencies are 12.1% and 13.3%, respectively (Fig. 3b). A statistical analysis of the photovoltaic parameters of 54 devices shows the reproducibility of high-performance $Rb_{0.15}Cs_{0.85}PbI_{1.75}Br_{1.25}$ devices (Fig. 3c). The $Rb_{0.15}Cs_{0.85}PbI_{1.75}Br_{1.25}$ device with suppressed LIPS shows improved operational stability compared with the $CsPbI_{1.4}Br_{1.6}$ device (Supplementary Fig. 21 and Supplementary Note 9 for a detailed discussion). The quasi-Fermi level splitting (QFLS) of the partially complete device stacks (ITO glass/NiO_x/Me-4PACz/perovskites) of these perovskites shows that the $Rb_{0.15}Cs_{0.85}PbI_{1.75}Br_{1.25}$ sample has a high QFLS (1.417 ± 0.004 eV) with a narrow spatial distribution compared with the $CsPbI_{1.4}Br_{1.6}$ perovskite (1.318 ± 0.054 eV) (Fig. 3d), which is indicative of reduced non-radiative recombination[36]. The Urbach energy values obtained from photothermal deflection spectroscopy (PDS) measurements decrease from 45 meV for $CsPbI_{1.4}Br_{1.6}$ to 31 meV for $Rb_{0.15}Cs_{0.85}PbI_{1.75}Br_{1.25}$ perovskite films (Fig. 3e). This suggests decreased electronic disorder of $Rb_{0.15}Cs_{0.85}PbI_{1.75}Br_{1.25}$ perovskite films, consistent with suppressed LIPS and improved perovskite film quality (Supplementary Note 10 for a detailed discussion)[37,38]. These are correlative with the high V_{OC} observed for the $Rb_{0.15}Cs_{0.85}PbI_{1.75}Br_{1.25}$ device[36,37].

All-perovskite triple-junction solar cells

We further employed the approximately 2.0-eV Rb/Cs mixed-cation inorganic perovskite as the absorber for the top subcell in a monolithic

all-perovskite TJSC. The configuration of the TJSC is ITO glass/NiO_x/Me-4PACz/2.0-eV inorganic perovskite (170 nm)/PEAI–$EDAI_2$/PCBM/PEIE/SnO_x/ITO/NiO_x/Me-4PACz/1.6-eV perovskite (780 nm)/PEAI–$EDAI_2$/PCBM/PEIE/SnO_x/gold (Au)/poly(3,4-ethylenedioxythiophene) polystyrene sulfonate (PEDOT:PSS)/1.22-eV SnPb perovskite (870 nm)/C_{60}/SnO_x/Ag (Fig. 4a). Figure 4b shows the *J*–*V* curves of a champion all-perovskite TJSC. The PCE from the reverse scan is 24.33% with a V_{OC} of 3.215 V, a short-circuit current (J_{SC}) of 9.71 mA cm^{-2} and a fill factor (FF) of 77.93%. There is negligible hysteresis between the forward and reverse *J*–*V* scans of the device (Fig. 4b). We achieved a certified quasi-steady-state PCE of 23.29% in an accredited independent PV calibration laboratory (National Renewable Energy Laboratory (NREL); Fig. 4c and Supplementary Fig. 22), which is, to our knowledge, the first reported certified PCE for perovskite-based TJSCs. The SPO efficiency over 20 min is 24.1% (Supplementary Fig. 23). The integrated J_{SC} values for the approximately 2.0-eV, approximately 1.6-eV and approximately 1.22-eV cells from external quantum efficiency (EQE) measurements of a TJSC are 10.18 mA cm^{-2}, 9.95 mA cm^{-2} and 9.31 mA cm^{-2}, respectively (Fig. 4d). The *J*–*V* performance from 32 devices is detailed in Supplementary Fig. 24. The efficiency of all-perovskite TJSCs will further improve through the development of new passivation strategies, improved interfacial contact and the optimization of light management (Supplementary Table 11 and Supplementary Note 11 for a detailed discussion).

We tracked the PCE of an encapsulated device stored in a nitrogen glovebox. After 120 days, the PCE shows a negligible decline (Supplementary Fig. 23). We also monitored the performance of an encapsulated TJSC under maximum-power-point tracking conditions and continuous AM 1.5G 1-sun illumination at room temperature in an ambient atmosphere (Fig. 4e). The optimized device based on a Rb/Cs mixed-cation perovskite retains 80% of its initial PCE after 420 h of continuous operation. Further analysis shows that 2.0-eV Rb/Cs perovskites undergo phase segregation after 450 h of maximum-power-point tracking (Supplementary Fig. 25, Supplementary Table 12 and Supplementary Note 12 for a detailed discussion). These results indicate that, although Rb incorporation offers a promising route to decreased light-induced phase segregation, the topic will benefit from further study along the path to a long-term operating lifetime solution.

Online content

Any methods, additional references, Nature Portfolio reporting summaries, source data, extended data, supplementary information, acknowledgements, peer review information; details of author contributions and competing interests; and statements of data and code availability are available at https://doi.org/10.1038/s41586-023-06006-7.

1. Stoumpos, C. C., Malliakas, C. D. & Kanatzidis, M. G. Semiconducting tin and lead iodide perovskites with organic cations: phase transitions, high mobilities, and near-infrared photoluminescent properties. *Inorg. Chem.* **52**, 9019–9038 (2013).
2. Eperon, G. E., Hörantner, M. T. & Snaith, H. J. Metal halide perovskite tandem and multiple-junction photovoltaics. *Nat. Rev. Chem.* **1**, 0095 (2017).
3. Hoke, E. T. et al. Reversible photo-induced trap formation in mixed-halide hybrid perovskites for photovoltaics. *Chem. Sci.* **6**, 613–617 (2015).
4. McMeekin, D. P. et al. A mixed-cation lead mixed-halide perovskite absorber for tandem solar cells. *Science* **351**, 151–155 (2016).
5. Abdi-Jalebi, M. et al. Maximizing and stabilizing luminescence from halide perovskites with potassium passivation. *Nature* **555**, 497–501 (2018).
6. Xiao, K. et al. Solution-processed monolithic all-perovskite triple-junction solar cells with efficiency exceeding 20%. *ACS Energy Lett.* **5**, 2819–2826 (2020).
7. Henry, C. H. Limiting efficiencies of ideal single and multiple energy gap terrestrial solar cells. *J. Appl. Phys.* **51**, 4494–4500 (1980).
8. Shockley, W. & Queisser, H. J. Detailed balance limit of efficiency of p-n junction solar cells. *J. Appl. Phys.* **32**, 510–519 (1961).
9. Pazos-Outon, L. M. et al. Photon recycling in lead iodide perovskite solar cells. *Science* **351**, 1430–1433 (2016).
10. Best research-cell efficiencies. *NREL* https://www.nrel.gov/pv/cell-efficiency.html (2022).
11. Green, M. A. et al. Solar cell efficiency tables (version 60). *Prog. Photovolt. Res. Appl.* **30**, 687–701 (2022).
12. Kojima, A., Teshima, K., Shirai, Y. & Miyasaka, T. Organometal halide perovskites as visible-light sensitizers for photovoltaic cells. *J. Am. Chem. Soc.* **131**, 6050–6051 (2009).
13. Lee, M. M., Teuscher, J., Miyasaka, T., Murakami, T. N. & Snaith, H. J. Efficient hybrid solar cells based on meso-superstructured organometal halide perovskites. *Science* **338**, 643–647 (2012).
14. Kim, H. S. et al. Lead iodide perovskite sensitized all-solid-state submicron thin film mesoscopic solar cell with efficiency exceeding 9%. *Sci. Rep.* **2**, 591 (2012).
15. Xu, J. et al. Triple-halide wide-band gap perovskites with suppressed phase segregation for efficient tandems. *Science* **367**, 1097–1104 (2020).
16. Hörantner, M. T. et al. The potential of multijunction perovskite solar cells. *ACS Energy Lett.* **2**, 2506–2513 (2017).
17. McMeekin, D. P. et al. Solution-processed all-perovskite multi-junction solar cells. *Joule* **3**, 387–401 (2019).
18. Wang, J. et al. 16.8% monolithic all-perovskite triple-junction solar cells via a universal two-step solution process. *Nat. Commun.* **11**, 5254 (2020).
19. Zheng, J. et al. Monolithic perovskite–perovskite–silicon triple-junction tandem solar cell with an efficiency of over 20%. *ACS Energy Lett.* **7**, 3003–3005 (2022).
20. Muscarella, L. A. et al. Lattice compression increases the activation barrier for phase segregation in mixed-halide perovskites. *ACS Energy Lett.* **5**, 3152–3158 (2020).
21. Rehman, W. et al. Photovoltaic mixed-cation lead mixed-halide perovskites: links between crystallinity, photo-stability and electronic properties. *Energy Environ. Sci.* **10**, 361–369 (2017).
22. Beal, R. E. et al. Cesium lead halide perovskites with improved stability for tandem solar cells. *J. Phys. Chem. Lett.* **7**, 746–751 (2016).
23. Brennan, M. C., Draguta, S., Kamat, P. V. & Kuno, M. Light-induced anion phase segregation in mixed halide perovskites. *ACS Energy Lett.* **3**, 204–213 (2017).
24. Noh, J. H., Im, S. H., Heo, J. H., Mandal, T. N. & Seok, S. I. Chemical management for colorful, efficient, and stable inorganic-organic hybrid nanostructured solar cells. *Nano Lett.* **13**, 1764–1769 (2013).
25. Yuan, Y. B. & Huang, J. S. Ion migration in organometal trihalide perovskite and its impact on photovoltaic efficiency and stability. *Acc. Chem. Res.* **49**, 286–293 (2016).
26. Beal, R. E. et al. Structural origins of light-induced phase segregation in organic–inorganic halide perovskite photovoltaic materials. *Matter* **2**, 207–219 (2020).
27. Marronnier, A. et al. Anharmonicity and disorder in the black phases of cesium lead iodide used for stable inorganic perovskite solar cells. *ACS Nano* **12**, 3477–3486 (2018).
28. Zhou, W. et al. Light-independent ionic transport in inorganic perovskite and ultrastable Cs-based perovskite solar cells. *J. Phys. Chem. Lett.* **8**, 4122–4128 (2017).
29. Kubicki, D. J., Stranks, S. D., Grey, C. P. & Emsley, L. NMR spectroscopy probes microstructure, dynamics and doping of metal halide perovskites. *Nat. Rev. Chem.* **5**, 624–645 (2021).
30. Kubicki, D. J. et al. Phase segregation in Cs-, Rb- and K-doped mixed-cation $(MA)_x(FA)_{1-x}PbI_3$ hybrid perovskites from solid-state NMR. *J. Am. Chem. Soc.* **139**, 14173–14180 (2017).
31. Xiao, J. W. et al. Stabilizing $RbPbBr_3$ perovskite nanocrystals through Cs^+ substitution. *Chem. Eur. J.* **25**, 2597–2603 (2019).
32. Stoumpos, C. C. & Kanatzidis, M. G. The renaissance of halide perovskites and their evolution as emerging semiconductors. *Acc. Chem. Res.* **48**, 2791–2802 (2015).
33. Linaburg, M. R., McClure, E. T., Majher, J. D. & Woodward, P. M. $Cs_{1-x}Rb_xPbCl_3$ and $Cs_{1-x}Rb_xPbBr_3$ solid solutions: understanding octahedral tilting in lead halide perovskites. *Chem. Mater.* **29**, 3507–3514 (2017).
34. Deng, Y. et al. Defect compensation in formamidinium–caesium perovskites for highly efficient solar mini-modules with improved photostability. *Nat. Energy* **6**, 633–641 (2021).
35. Eames, C. et al. Ionic transport in hybrid lead iodide perovskite solar cells. *Nat. Commun.* **6**, 7497 (2015).
36. El-Hajje, G. et al. Quantification of spatial inhomogeneity in perovskite solar cells by hyperspectral luminescence imaging. *Energy Environ. Sci.* **9**, 2286–2294 (2016).
37. Subedi, B. et al. Urbach energy and open-circuit voltage deficit for mixed anion–cation perovskite solar cells. *ACS Appl. Mater. Interfaces* **14**, 7796–7804 (2022).
38. Mahesh, S. et al. Revealing the origin of voltage loss in mixed-halide perovskite solar cells. *Energy Environ. Sci.* **13**, 258–267 (2020).

Methods

Materials

All materials were used as received without further purification. Lead iodide (PbI_2, 99.99%), lead bromide ($PbBr_2$, 99.999%) and Me-4PACz were purchased from TCI chemicals. Caesium iodide (CsI, 99.999%), caesium bromide (CsBr, >99.9%), rubidium bromide (RbBr, 99.6%), tin(II) iodide (SnI_2, 99.99%, Beads), tin(II) fluoride (SnF_2, 99%), glycine hydrochloride (99%), guanidine thiocyanate (GuaSCN, 99%), $EDAI_2$ (98%), polyethyleneimine, 80% ethoxylated solution (PEIE, 37 wt% in water), nickel(II) nitrate hexahydrate ($Ni(NO_3)_2{\cdot}6H_2O$, 99.999%) and sodium hydroxide (NaOH, ≥99.99%) were purchased from Sigma-Aldrich. Methylammonium iodide (MAI), formamidinium iodide (FAI), formamidinium chloride (FACl) and PEAI were purchased from GreatCell Solar Materials. PCBM (99.5%) and C_{60} were purchased from Nano-C. Tetrakis(dimethylamino) tin(IV) (99.99%-Sn, 50–1815 Tin) was purchased from Strem Chemicals.

Dimethyl sulfoxide (DMSO, 99.9%), *N*,*N*-dimethylformamide (DMF, 99.8%), 2-propanol (IPA, 99.5%), chlorobenzene (CB, 99.8%), anisole (99.7%) and 1-propanol (99.7%) were purchased from Sigma-Aldrich. Toluene (99.8%) was purchased from Alfa Aesar. PEDOT:PSS aqueous solution (Al-4083) was purchased from Ossila. Commercial ITO substrates (20 Ω sq^{-1}) with 25 mm × 25 mm dimension were purchased from TFD. Quartz substrates were purchased from Shenzhen Weina Technology Electronic.

Preparation of inorganic perovskite precursor solutions

The precursor chemicals were mixed stoichiometrically with anhydrous dimethyl sulfoxide solvent and stirred until completely dissolved. Before use, the perovskite precursor solution was filtered through a 0.22-μm polytetrafluoroethylene (PTFE) membrane.

FACl (FACl:Pb^{2+} = 0.1 mmol:1 mmol) was added into the I/Br mixed precursor solutions as an additive to improve the interfacial contact of inorganic perovskite and substrate[39]. FACl was evaporated during the annealing process at 180 °C (Supplementary Fig. 9)[40]. For simplicity, we do not show the 0.1 mmol FACl additive and 1 ml DMSO in the following recipes.

1 M $Rb_{0.15}Cs_{0.85}PbI_{1.75}Br_{1.25}$ = 0.15 mmol RbI + 0.85 mmol CsI + 0.375 mmol PbI_2 + 0.625 mmol $PbBr_2$

1 M $CsPbI_{1.4}Br_{1.6}$ = 1 mmol CsI + 0.2 mmol PbI_2 + 0.8 mmol $PbBr_2$

1 M $CsPbI_{1.75}Br_{1.25}$ = 1 mmol CsI + 0.375 mmol PbI_2 + 0.625 mmol $PbBr_2$

1 M $RbPbI_{1.75}Br_{1.25}$ = 1 mmol RbI + 0.375 mmol PbI_2 + 0.625 mmol $PbBr_2$

1 M $CsPbI_2Br$ = 1 mmol CsI + 0. 5 mmol PbI_2 + 0.5 mmol $PbBr_2$

1 M $RbPbI_2Br$ = 1 mmol RbI + 0. 5 mmol PbI_2 + 0.5 mmol $PbBr_2$

1 M $CsPbI_{1.5}Br_{1.5}$ = 1 mmol CsI + 0. 25 mmol PbI_2 + 0.75 mmol $PbBr_2$

1 M $RbPbI_{1.5}Br_{1.5}$ = 1 mmol RbI + 0. 25 mmol PbI_2 + 0.75 mmol $PbBr_2$

For pure-Br precursor solutions, the concentration was 0.5 M without additives because 1 M cannot be dissolved in DMSO.

0.5 M $CsPbBr_3$ = 0.5 mmol CsBr + 0.5 mmol $PbBr_2$

0.5 M $RbPbBr_3$ = 0.5 mmol RbBr + 0.5 mmol $PbBr_2$

DMAI (DMAI:Pb^{2+} = 1 mmol:1 mmol) was added into the following pure-I precursor solutions as an additive to promote the formation of pure-I inorganic perovskites[41]. DMAI was evaporated during the annealing process at 250 °C (ref. 42). For simplicity, we do not show the 1 mmol DMAI additive and 1 ml DMSO in the following recipes.

1 M $CsPbI_3$ = 1 mmol CsI + 1 mmol PbI_2

1 M $RbPbI_3$ = 1 mmol RbI + 1 mmol PbI_2

$Rb_xCs_{1-x}PbX_3$ (where X is I or Br) precursor solutions can be obtained by mixing the $CsPbX_3$ and $RbPbX_3$ precursor solutions based on volume ratios.

NiO_x nanoparticle synthesis

The NiO_x nanoparticles were prepared by hydrolysis of nickel nitrate following previous work[43]. Briefly, $Ni(NO_3)_2{\cdot}6H_2O$ (20 mmol) was dissolved in deionized water (20 ml) to obtain a dark-green solution. Then, NaOH aqueous solution (4 ml, 10 M) was slowly added to the dark-green solution with stirring. After stirring for 20 min, the colloidal precipitate was washed thoroughly using deionized water three times and dried at 80 °C for 6 h. The obtained green powder was then calcined at 270 °C for 2 h to obtain a black powder. The NiO_x nanoparticle ink was prepared by dispersing the obtained NiO_x nanoparticles in a mixed solution of deionized water and IPA (3:1, v/v) for a concentration of 5 mg ml^{-1}.

Inorganic perovskite device fabrication

The configuration of inorganic perovskite devices was ITO glass/NiO_x/Me-4PACz/inorganic perovskite/PEAI–$EDAI_2$/PCBM/PEIE/SnO_x/Ag.

The pre-patterned ITO glasses were sequentially sonicated in acetone and IPA each for 20 min. After drying with nitrogen, the substrates were exposed to UV-ozone treatment for 20 min to remove organic contaminants.

NiO_x layers were prepared by spin-coating 100 μl NiO_x nanoparticle solution on ITO substrates at 3,000 rpm for 25 s in the air without any post-treatment, then immediately transferred to a nitrogen-filled glovebox.

For the Me-4PACz layer, 100 μl Me-4PACz (0.5 mg ml^{-1}) solution in ethanol was spin-coated on the NiO_x film at 3,000 rpm for 30 s in a nitrogen-filled glovebox. Then the prepared film was annealed at 100 °C for 10 min.

For Br-based or I/Br mixed perovskite films, 100 μl inorganic perovskite precursor solution was spin-coated on the substrate at 3,000 rpm for 70 s. The film was firstly annealed at 40 °C until the colour of the film started to turn brown (5–20 s in our lab), then quickly moved to a 180 °C hotplate for 5-min annealing. For pure-I-based inorganic perovskite, 100 μl inorganic perovskite precursor solution was spin-coated on the substrate at 3,000 rpm for 70 s. Then the film was annealed at 250 °C for 5 min.

For the PEAI–$EDAI_2$ modified layer, the treatment solution was prepared by dissolving 1 mg PEAI and 1 mg $EDAI_2$ into 1 ml IPA. Then 130 μl filtered solution was spin-coated on the inorganic perovskite film at 4,000 rpm for 25 s. Then the film was annealed at 100 °C for 5 min.

For the PCBM layers, 70 μl PCBM (15 mg ml^{-1}) solution in CB was spin-coated on the inorganic perovskite/PEAI–$EDAI_2$ film at 1,000 rpm for 30 s.

For the PEIE layers, 100 μl PEIE (0.025 wt%) solution in IPA was spin-coated on the PCBM film at 4,000 rpm for 30 s.

For the SnO_x layer, the film was then transferred to the atomic layer deposition system (Picosun) to deposit 20-nm SnO_x at 100 °C using precursors of tetrakis(dimethylamino) tin(IV) (99.9999%) and deionized water.

The 140-nm-thick Ag electrode was deposited by thermal evaporation.

Fabrication of all-perovskite triple-junction solar cells

The configuration of the triple-junction solar cells was ITO/NiO_x/Me-4PACz/2.0-eV inorganic perovskite (170 nm)/PEAI–$EDAI_2$/PCBM/PEIE/SnO_x/ITO/NiO_x/Me-4PACz/1.6-eV perovskite (780 nm)/PEAI–$EDAI_2$/PCBM/PEIE/SnO_x/Au/PEDOT:PSS/1.22-eV SnPb perovskite (870 nm)/C_{60}/SnO_x/Ag.

For the approximately 2.0-eV inorganic perovskite top cell, the fabrications of ITO glass, NiO_x, Me-4PACz, PEAI–$EDAI_2$, PCBM, PEIE and SnO_x layers were the same as inorganic perovskite single-junction devices. The PEIE layer can increase the compatibility of SnO_x, which can protect the perovskite layer from degradation when spin-coating the following NiO_x and perovskite layers[44]. For the 2.0-eV inorganic perovskite layers, 100 μl 0.8 M $Rb_{0.15}Cs_{0.85}PbI_{1.75}Br_{1.25}$ inorganic perovskite precursor solution was spin-coated on the substrate at 3,000 rpm for 70 s. The film was first annealed at 40 °C for 15 s, then quickly moved to a 180 °C hotplate for 5 min.

For the ITO layer, the top cell was then transferred to the radio-frequency magnetron sputtering system. The ITO target used in

this study was a commercial grade of purity of >99.99% with a size of 3.00″ diameter × 0.125″ thick. The target composition was In_2O_3/SnO_2 90/10 wt%. The process pressure was 3 mtorr at an argon flow of 18 standard cubic centimetres per minute. The average deposition rate was about 0.24 A s^{-1} at 33 W power. A total ITO layer thickness of 20 nm was deposited.

For the approximately 1.6-eV perovskite middle cell, the fabrication procedures of the NiO_x, Me-4PACz, PEAI–$EDAI_2$, PCBM, PEIE and SnO_x layers were similar to those described above for the single-junction inorganic perovskite devices. The only difference was that the subcell was treated by plasma etching for 30 s to increase its surface wettability before spin-coating the NiO_x nanoparticle solution. For the 1.6-eV perovskite film, the $Cs_{0.05}FA_{0.9}MA_{0.05}Pb(I_{0.9}Br_{0.1})_3$ perovskite precursor solution (1.5 M) was prepared by dissolving 0.075 mmol CsI, 0.075 mmol MABr, 1.35 mmol FAI, 0.1875 mmol $PbBr_2$ and 1.3125 mmol PbI_2 in a mixed solvent of DMF and DMSO with a volume ratio of 4:1. The perovskite precursor solution was filtered through a 0.22-μm PTFE membrane before use. Then 100 μl of perovskite solution was dropped on the substrate and spin-coated at 1,000 rpm for 10 s followed by 5,000 rpm for 30 s. Then 150 μl anisole was dropped onto the substrate at the last 5 s of the spin-coating, resulting in the formation of dark brown films that were then annealed on a hotplate at 100 °C for 10 min.

A 1-nm-thick Au electrode was deposited by thermal evaporation.

For the approximately 1.22-eV SnPb perovskite bottom cell, the PEDOT:PSS layer was prepared by spin-coating 100 μl diluted PEDOT:PSS solution with *n*-propanol at a volume ratio of 1:1 on the substrate at 4,000 rpm for 30 s and then annealing at 100 °C for 15 min in ambient air. After cooling, the substrates were immediately transferred to a nitrogen-filled glovebox to deposit perovskite films. A 1.8 M SnPb perovskite precursor solution with a composition of $Cs_{0.05}FA_{0.7}MA_{0.25}Pb_{0.5}Sn_{0.5}I_3-0.05SnF_2$ was prepared by dissolving 0.09 mmol CsI, 1.26 mmol FAI, 0.45 mmol MAI, 0.9 mmol SnI_2, 0.9 mmol PbI_2 and 0.09 mmol SnF_2 in a 1 ml mixed solvent of DMF and DMSO with a volume ratio of 3:1. Tin powders (5 mg), GuaSCN (4 mg), 4F-PEABr (2 mg) and glycine hydrochloride (4 mg) were added to the precursor solution. The precursor solution was then stirred at room temperature for 1 h. The precursor solution was filtered using a 0.22-μm PTFE membrane before deposition. Then 70 μl of perovskite solution was deposited on the substrate and spin-coated with a two-step spin-coating procedure: 1,000 rpm for 10 s and 3,800 rpm for 45 s. Then 300 μl CB was dropped onto the substrate during the second spin-coating step at the last 20 s of the spin-coating. The substrates were then annealed at 100 °C for 10 min. Finally, 20-nm C_{60}, 20-nm SnO_x and 140-nm Ag were sequentially deposited on the top of SnPb perovskite layer by organic thermal evaporation, atomic layer deposition and metal thermal evaporation, respectively.

Reporting summary

Further information on research design is available in the Nature Portfolio Reporting Summary linked to this article.

Data availability

All data are available in the paper or its Supplementary Information. The crystallographic files (CIF) for the compounds reported in this work can be found as depositions in the Cambridge Crystallographic Data Centre (CCDC) based on the following deposition numbers: 2211086 ($CsPbI_{1.46}Br_{1.54}$), 2211087 ($CsPbI_{1.73}Br_{1.27}$) and 2211088 ($Rb_{0.22}Cs_{0.78}PbI_{1.65}Br_{1.35}$).

Code availability

The codes and post-analysis tools for calculations are available from the FHI-aims website: https://fhi-aims.org.

39. Zhang, J. et al. Intermediate phase enhances inorganic perovskite and metal oxide interface for efficient photovoltaics. *Joule* **4**, 222–234 (2020).
40. Wang, Z. et al. Additive-modulated evolution of $HC(NH_2)_2PbI_3$ black polymorph for mesoscopic perovskite solar cells. *Chem. Mater.* **27**, 7149–7155 (2015).
41. Wang, Y. et al. Thermodynamically stabilized β-$CsPbI_3$-based perovskite solar cells with efficiencies >18%. *Science* **365**, 591–595 (2019).
42. Meng, H. et al. Chemical composition and phase evolution in DMAI-derived inorganic perovskite solar cells. *ACS Energy Lett.* **5**, 263–270 (2019).
43. Chen, H. et al. Quantum-size-tuned heterostructures enable efficient and stable inverted perovskite solar cells. *Nat. Photon.* **16**, 352–358 (2022).
44. Palmstrom, A. F. et al. Enabling flexible all-perovskite tandem solar cells. *Joule* **3**, 2193–2204 (2019).

Acknowledgements This research was made possible by a US Department of the Navy, Office of Naval Research grant (N00014-20-1-2572), and the US Department of Energy's Office of Energy Efficiency and Renewable Energy (EERE) under the Solar Energy Technologies Office Award Number DE-EE0008753. This work was supported in part by the Ontario Research Fund-Research Excellence programme (ORF7-Ministry of Research and Innovation, Ontario Research Fund-Research Excellence Round 7). M.G.K. was supported by the Office of Naval Research (ONR) under grant N00014-20-1-2725. At King Abdullah University of Science and Technology (KAUST), this work was supported by the under award no. OSR-2020-CRG9-4350.2. This work was also supported by the Natural Sciences and Engineering Council of Canada and the Vanier Canada Graduate Scholarship. Z.W. acknowledges the Banting Postdoctoral Fellowships Program of Canada. D.J.K. acknowledges the support of the University of Warwick. The UK High-Field Solid-State NMR Facility used in this research was funded by EPSRC and BBSRC (EP/T015063/1), as well as the University of Warwick, including via part funding through Birmingham Science City Advanced Materials Projects 1 and 2 supported by Advantage West Midlands (AWM) and the European Regional Development Fund (ERDF). The crystallographic experiments made use of the IMSERC Crystallography and Physical Characterization facilities at Northwestern University, which received support from the Soft and Hybrid Nanotechnology Experimental (SHyNE) Resource (NSF ECCS-2025633), and Northwestern University. The purchase of the Ag-microsource used to collect both single and powder diffraction data was supported by the Major Research Instrumentation Program for the National Science Foundation under the award CHE-1920248. This work also made use of the EPIC facility at Northwestern University's NUANCE Center, which has received support from the SHyNE Resource (NSF ECCS-2025633), the IIN and Northwestern's MRSEC programme (NSF DMR-1720139). Computations were performed on the Niagara supercomputer at the SciNet HPC Consortium. SciNet is funded by the Canada Foundation for Innovation; the Government of Ontario; Ontario Research Fund Research Excellence; and the University of Toronto. A.B. was supported, in part, by a fellowship through the National Defense Science and Engineering Graduate (NDSEG) Fellowship Program, sponsored by the Air Force Research Laboratory (AFRL), the Office of Naval Research (ONR) and Army Research Office (ARO). We thank Tao Song for efficiency certification in NREL. Z.W. thanks Yicheng Zhao, Zhenyi Ni and Emre Yengel for discussion about LIPS. A.B. acknowledges Christos D. Malliakas for assistance with the single-crystal measurements and discussions and thanks Abishek K. Iyler, Craig Laing and Michael Quintero for discussions.

Author contributions Z.W. conceived the idea of this project. L.Z. and Z.W. fabricated the 2.0-eV bandgap devices and triple-junction solar cells for performance and fabricated the perovskite films for characterizations. H.C., L.Z. and Z.W. fabricated the 1.6-eV bandgap cells. L.Z., Z.W., A.M. and C.L. fabricated the 1.22-eV bandgap cells. T.Z. carried out the DFT calculations and analysed the data. H.C. prepared NiO_x nanoparticles and developed the surface passivation of the inorganic perovskite layers and 1.6-eV perovskite layers. B.C. helped with experimental design and data analysis. D.J.K. carried out the solid-state NMR characterization, prepared the corresponding powders and analysed the data. A.B. prepared the crystals and carried out the crystal XRD and data analysis. C.L. carried out EQE measurements. E.U. carried out the PL mapping and QFLS analysis. R.d.R. and M.C. carried out the TEM-EDS and data analysis. G.Y. measured transient ion-migration currents and carried out data analysis. B.S. performed PDS characterizations and data analysis. D.L. and J. Hu carried out the depth-profile X-ray photoelectron spectroscopy characterization and data analysis. S.D.W. carried out the atomic force microscopy characterization. L.Z. and Z.W. carried out the UV–vis measurements, XRD measurements, PL measurements, *J*–*V* measurements and stability measurements. Z.W. wrote the original draft. E.H.S., L.W., T.Z., D.J.K. and A.M., helped to review and edit the manuscript. E.H.S. secured funding. All the authors contributed to the discussion of the results and the final manuscript preparation.

Competing interests The authors declare no competing interests.

Additional information

Supplementary information The online version contains supplementary material available at https://doi.org/10.1038/s41586-023-06006-7.

Correspondence and requests for materials should be addressed to Edward H. Sargent.

Peer review information *Nature* thanks Michael McGehee and the other, anonymous, reviewer(s) for their contribution to the peer review of this work. Peer reviewer reports are available.

nature research

Corresponding author(s): Edward Sargent

Solar Cells Reporting Summary

Nature Research wishes to improve the reproducibility of the work that we publish. This form is intended for publication with all accepted papers reporting the characterization of photovoltaic devices and provides structure for consistency and transparency in reporting. Some list items might not apply to an individual manuscript, but all fields must be completed for clarity.

For further information on Nature Research policies, including our data availability policy, see Authors & Referees.

Experimental design

Please check: are the following details reported in the manuscript?

1. Dimensions

Area of the tested solar cells	☒ Yes ☐ No	Device testing in Methods
Method used to determine the device area	☒ Yes ☐ No	Device testing in Methods

2. Current-voltage characterization

Current density-voltage (J-V) plots in both forward and backward direction	☒ Yes ☐ No	Figure 4b & Supplementary Fig. 21
Voltage scan conditions *For instance: scan direction, speed, dwell times*	☒ Yes ☐ No	Figure 3a & 4b & Supplementary Fig. 21
Test environment *For instance: characterization temperature, in air or in glove box*	☒ Yes ☐ No	Device testing in Methods
Protocol for preconditioning of the device before its characterization	☒ Yes ☐ No	Solar cell fabrication and device testing in Methods
Stability of the J-V characteristic *Verified with time evolution of the maximum power point or with the photocurrent at maximum power point; see ref. 7 for details.*	☒ Yes ☐ No	Stability testing in Methods, Figure 4e & Supplementary Fig. 21

3. Hysteresis or any other unusual behaviour

Description of the unusual behaviour observed during the characterization	☐ Yes ☒ No	Negligible hysteresis
Related experimental data	☒ Yes ☐ No	Throughout main text and supplementary information

4. Efficiency

External quantum efficiency (EQE) or incident photons to current efficiency (IPCE)	☒ Yes ☐ No	Figure 4d
A comparison between the integrated response under the standard reference spectrum and the response measure under the simulator	☒ Yes ☐ No	Certified results in Figure 4c & supplementary figure 22
For tandem solar cells, the bias illumination and bias voltage used for each subcell	☒ Yes ☐ No	Device testing in methods

5. Calibration

Light source and reference cell or sensor used for the characterization	☒ Yes ☐ No	Device testing in methods
Confirmation that the reference cell was calibrated and certified	☒ Yes ☐ No	Device testing in methods

Calculation of spectral mismatch between the reference cell and the devices under test	☒ Yes ☐ No	Device testing in methods

6. Mask/aperture

Size of the mask/aperture used during testing	☒ Yes ☐ No	Device testing in methods
Variation of the measured short-circuit current density with the mask/aperture area	☒ Yes ☐ No	Figure 3a, 4b, Supplementary Figure 21, 25

7. Performance certification

Identity of the independent certification laboratory that confirmed the photovoltaic performance	☒ Yes ☐ No	Main text, Figure 4c , Supplementary Figure 21
A copy of any certificate(s) *Provide in Supplementary Information*	☒ Yes ☐ No	Supplementary Figure 22

8. Statistics

Number of solar cells tested	☒ Yes ☐ No	Figure 3c, Supplementary Figure 24
Statistical analysis of the device performance	☒ Yes ☐ No	Figure 3c, Supplementary Figure 24

9. Long-term stability analysis

Type of analysis, bias conditions and environmental conditions *For instance: illumination type, temperature, atmosphere humidity, encapsulation method, preconditioning temperature*	☒ Yes ☐ No	Fig 4e, Supplementary Figure 21 and 23, 25. stability testing in methods